nature research
https://doi.org/10.1038/s41928-020-00466-9

Supplementary information

A low-power biomimetic collision detector based on an in-memory molybdenum disulfide photodetector

In the format provided by the
authors and unedited

Supplementary Information

A low-power biomimetic collision detector based on in-memory molybdenum disulfide photodetector

Darsith Jayachandran[1,#], Aaryan Oberoi[1,#], Amritanand Sebastian[1], Tanushree H Choudhury[2], Balakrishnan Shankar[3], Joan M Redwing[2,4,5]

& Saptarshi Das[1,4,5,*]

[1]Department of Engineering Science and Mechanics, Pennsylvania State University, University Park, PA, 16802, USA

[2]2D Crystal Consortium – Materials Innovation Platform, Pennsylvania State University, University Park, PA, 16802, USA

[3]Department of Mechanical Engineering, Amrita School of Engineering, Amritapuri, Kerala 690525, India

[4]Department of Materials Science and Engineering, Pennsylvania State University, University Park, PA, 16802, USA

[5]Materials Research Institute, Pennsylvania State University, University Park, PA 16802, USA

[#] *Equal Contribution*

** Corresponding Author*

Supplementary Information 1.

Evolution of Biomimetic Collision Detectors						
Year	**Authors**	**Description**	**Model**	**Technology**	**Area**	**Energy Expenditure**
1986	J. Tanner, C. Mead [1]	1) Analogue photosensors coupled with constraint solving circuits and other motion detection circuitry. (Uniform motion detection) 2) 8 x 8 array chip		Analog VLSI	-	
1990	Andreas G. Andreou, Kim Strohbehn [2]	1) Position detection: Photoreceptors, resistive potential divider, and an aggregation circuit. 2) Motion computation: Each cell in the array consists of bipolar phototransistor, delay circuit and two multipliers.	Hassenstein-Reichardt-Poggio Models	Analog VLSI	1 cm x 1 cm	
1999	Reid R. Harrison, Christof Koch [3]	1) Photoreceptors, temporal bandpass filters, temporal lowpass filters, multipliers. 2) 34 transistors and 5 capacitors in one EMD. 3) The entire chip consists of 24 EMD opponent pairs.	Hassenstein-Reichardt	1.2 µm CMOS Analog VLSI	2 mm x 2 mm	1 mW
1995	D. Abbott *et al.* [4]	1D linear array of 60 photodetectors with 60 channels of parallel analogue differentiators.	Template model	2 µm CMOS Analog VLSI	4.5 mm x 4.6 mm	
1997	A. Moini *et al.* [5]	1) Two arrays of analogue circuitry each of 64 rows. 2) A row contains a photodetector, CMSA (Current Mode Spatial Averaging) cell, division circuit, differentiator, thresholding circuit and analogue switching circuits.	Template model	1.2 µm CMOS Analog VLSI	2 mm x 2 mm	
1996	A. Moini, A. Bouzerdoum, A. Yakovleff, and K. Eshraghian [6]	1) Each cell consists of a photo circuit, differentiator, a thresholding stage and digital latches. 2) The chip consists of 256 cells.	Template model	0.8 µm 3M-1P CMOS Analog VLSI	1.5 mm x 3.1 mm	

2009	H. Okuno and T. Yagi [7]	1) The system consists of a silicon retina. 2) 100x100 active pixel sensors, resistive networks, and differential amplifiers, analogue to digital converters and FPGA circuits. 3) Total gate count of 45000.				600 mW
2005	R. Takami, K. Shimonomura, S. Kameda, and T. Yagi [8]	1) A 100x100 pixel silicon retina. Each pixel consists of a photodiode and a source-follower circuit. 2) Silicon retina is coupled with digital interface module consisting of FPGA 3) 30000 gates and an 8-bit A/D converter.		0.25 µm CMOS	9.8 mm x 9.8 mm	3.6 µW/pixel
2005	R. R. Harrison [9]	1) A 17x17 array of pixels. Each pixel consists of a photoreceptor, LMC circuit, low pass “delay” filter and four correlators. 2) This is then coupled with leaky integrator and comparator (off chip components). 3) Able to detect collisions 100–400 ms before impact in complex, real-world scenes	Reichardt model.	0.5-m 2-poly,3-metal standard CMOS process	2.2 mm x 2.2 mm	140 µW
2012	M. Sarkar, D. S. S. Bello, C. van Hoof, and A. J. Theuwissen [10]	Each pixel of the image sensor consists of a photodiode, analogue comparator, two banks of analogue memories and two SRAMs for digital memory.		180 nm CMOS process	5 mm x 4 mm	
2018	C. Zhang, S. Lindner, I. M. Antolovic, M. Wolf, and E. Charbon [11]	An array of 32x32 pixels. The sensor is single-photon avalanche diode. 32 pixels in each column share 4 time-to-digital (TDC) architectures.		180 nm CMOS process	5 mm x 2 mm	0.31 W (for the LiDAR experiment)

Supplementary Information 2.

MoS_2 is one of the most studied layered two-dimensional (2D) material beyond graphene [12, 13]. It also represents a wider class of van der Waals (vdW) materials known as the transition metal dichalcogenides (TMDCs) [14]. The layered structure allows micromechanical separation of atomically thin standalone layers of MoS_2 where unique electronic properties emerge. Most important is the semiconducting nature that allows orders of magnitude modulation in the sheet conductance using electrostatic gate control owing to the existence of a finite bandgap which also aids in achieving low power operation. Furthermore, monolayer MoS_2 is a direct bandgap semiconductor that has enabled many photonic applications [15]. Early proof-of-concept studies on MoS_2 based optoelectronic devices have exploited exfoliation of monolayers from single crystal flakes. However, exfoliation is not a scalable technological solution and hence commercialization of MoS_2 based devices necessitates large-scale growth solutions.

In this study, we have utilized metal organic chemical vapor deposition (MOCVD) technique for the synthesis of large area monolayer MoS_2 films inside a cold-wall horizontal reactor setup using molybdenum hexacarbonyl, $Mo(CO)_6$, and H_2S as the precursor and H_2 as the carrier gas at 1000 ^{0}C on epitaxial sapphire substrate. Epitaxial growth at elevated temperature using hydride chalcogen precursor ensure better crystallinity [16] and low carbon contamination [17] in the MoS_2 film which ultimately results in better electrical performance. Fig. S1a shows a fully coalesced monolayer MoS_2 film on a 2-inch sapphire substrate. Following the synthesis, monolayer MoS_2 film was transferred from the sapphire substrate to the device fabrication substrate using a PMMA-assisted wet transfer process as shown in Fig. S1b [18]. Back gated field effect transistors (FET) are subsequently fabricated. The channel region was patterned using e-beam lithography and etched using sulfur hexafluoride (SF_6) at 5°C for 30 s. Source/drain contacts are also defined using

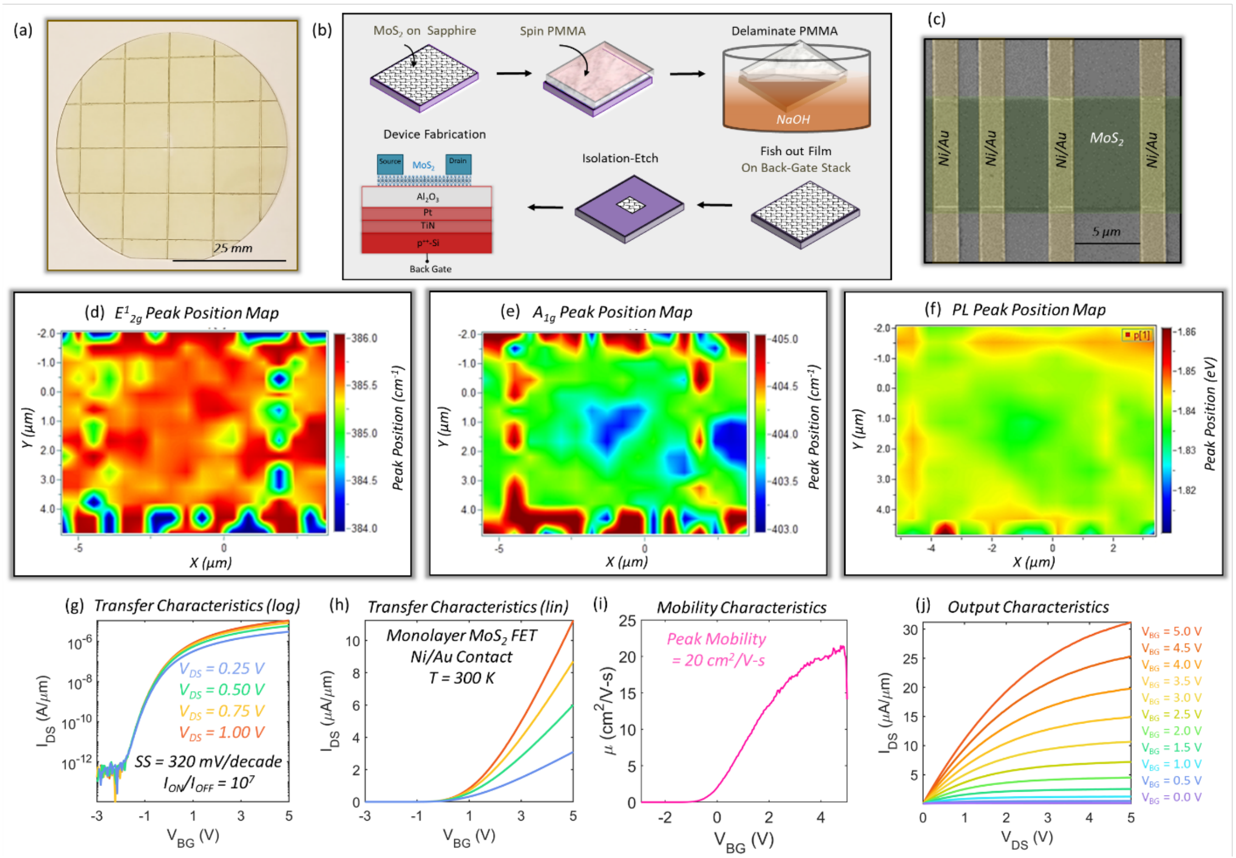

Figure S1. Monolayer MoS_2 Synthesis, Characterization and Device Fabrication. *a) A fully coalesced monolayer MoS_2 film on a 2-inch sapphire substrate grown using metal organic chemical vapor deposition (MOCVD) technique inside a cold-wall horizontal reactor setup using molybdenum hexacarbonyl, $Mo(CO)_6$, and H_2S as the precursor and H_2 as the carrier gas at 1000 ^{0}C. b) PMMA-assisted wet transfer process used for transferring the monolayer MoS_2 film from the sapphire substrate to the device fabrication substrate followed by back gated field effect transistors (FET) fabrication. The back-gate stack consisted of atomic layer deposition (ALD) grown 50 nm Al_2O_3 used as the gate dielectric and Pt/TiN/p^{++}-Si as the gate electrode. c) False colored scanning electron microscope (SEM) image of the monolayer MoS_2 FET. The device used as the collision detector has 1 μm channel length and 5 μm channel width. The transferred monolayer MoS_2 film quality was accessed using Raman spectroscopy and photoluminescence (PL) measurements. Spatial map of the peak position of two Raman active modes d) E_{2g}^1 and e) A_{1g} over 5 μm X 5 μm active device area show less than 0.5% variation indicating uniformity of the film. The peak separation of 18 cm^{-1} is also consistent with monolayer MoS_2. f) Map of PL peak position. Intense PL observed at 1.84 eV is attributed to the indirect to direct bandgap transition at the K-point in the Brillouin zone in monolayers MoS_2 and is severely suppressed in bulk MoS_2. Transfer characteristics, i.e. source to drain current (I_{DS}) as a function of the back gate voltage (V_{BG}) for the monolayer MoS_2 FET measured at different source to drain biases (V_{DS}) in the g) logarithmic and h) linear scales. The device shows excellent ON/OFF current ratio in excess of 10^7, subthreshold slope (SS) of less than 320 mV/decade, and none to minimal drain induced barrier lowering (DIBL). The threshold voltage (V_{TH}) was found to be ~0.45 V. i) The field effect mobility (μ_{FE}) extracted from the trans-conductance as a function of V_{BG}. The peak μ_{FE} was found to be ~20 cm^2/V-s, which is comparable to exfoliated single crystal monolayer MoS_2. j) Output characteristics (i.e. I_{DS} versus V_{DS} for different V_{BG}) of the MoS_2 FET with the ON current reaching as high as ~30 μA/μm at V_{DS} = 5 V for an inversion charge carrier density of ~$5*10^{12}/cm^2$.*

the e-beam lithography followed by e-beam evaporation of 40nm Ni/30nm Au stack. Fig. S1c shows the false colored scanning electron microscope (SEM) image of the monolayer MoS_2 FET. The device used as the collision detector has 1 μm channel length and 5 μm channel width. The back-gate stack consisted of atomic layer deposition (ALD) grown 50 nm Al_2O_3 used as the gate dielectric and Pt/TiN/p^{++}-Si as the gate electrode. The use of this particular back-gate stack will be explained later.

Before measuring the electrical response, we investigated the quality of the transferred monolayer MoS_2 using Raman spectroscopy and photoluminescence (PL) measurements. Fig. S1d and S1e, respectively show the spatial map of the peak position of two Raman active modes E_{2g}^1 and A_{1g} over 5 μm X 5 μm active device area. Raman peak positions vary less than 0.5% over the entire map confirming high quality and uniformity of the monolayer film. The peak separation of 18 cm^{-1} is also consistent with monolayer MoS_2 [19]. Furthermore, Fig. S1f shows uniform and intense PL peak at 1.84 eV which is attributed to the indirect to direct bandgap transition at the K-point in the Brillouin zone in monolayers MoS_2 and is severely suppressed in bulk MoS_2.

Fig. S1g and Fig. S1h show the transfer characteristics, i.e. source to drain current ($\boldsymbol{I_{DS}}$) as a function of the back gate voltage ($\boldsymbol{V_{BG}}$) for the monolayer MoS_2 FET measured at different source to drain biases ($\boldsymbol{V_{DS}}$) in the logarithmic and linear scales, respectively. Clearly, n-type transport dominates in monolayer MoS_2 FET which can be attributed to the pinning of metal Fermi level close to the conduction band facilitating electron injection [20, 21]. The device shows excellent ON/OFF current ratio in excess of 10^7, subthreshold slope (SS) of less than 320 mV/decade, none to minimal drain induced barrier lowering (DIBL), and low gate leakage indicating high quality of the gate dielectric, semiconducting MoS_2 channel, and dielectric and contact interfaces (see *Supplementary Information 3*). Combined, the device exhibits low voltage operation under 5 V for both the back-gate bias and drain bias. The threshold voltage ($\boldsymbol{V_{TH}}$) was found to be ~0.45 V and the field effect mobility ($\boldsymbol{\mu_{FE}}$) value was found to be ~20 cm^2/V-s extracted from the peak trans-conductance as shown in Fig. S1i. The $\boldsymbol{\mu_{FE}}$ value is comparable to exfoliated single crystal monolayer MoS_2. Fig. S1j shows the output characteristics (i.e. $\boldsymbol{I_{DS}}$ versus $\boldsymbol{V_{DS}}$ for different $\boldsymbol{V_{BG}}$) of the MoS_2 FET with the ON current reaching as high as ~30 µA/µm at $\boldsymbol{V_{DS}}$ = 5 V for an inversion charge carrier density of ~5*10^{12}/cm^2.

Supplementary Information 3.

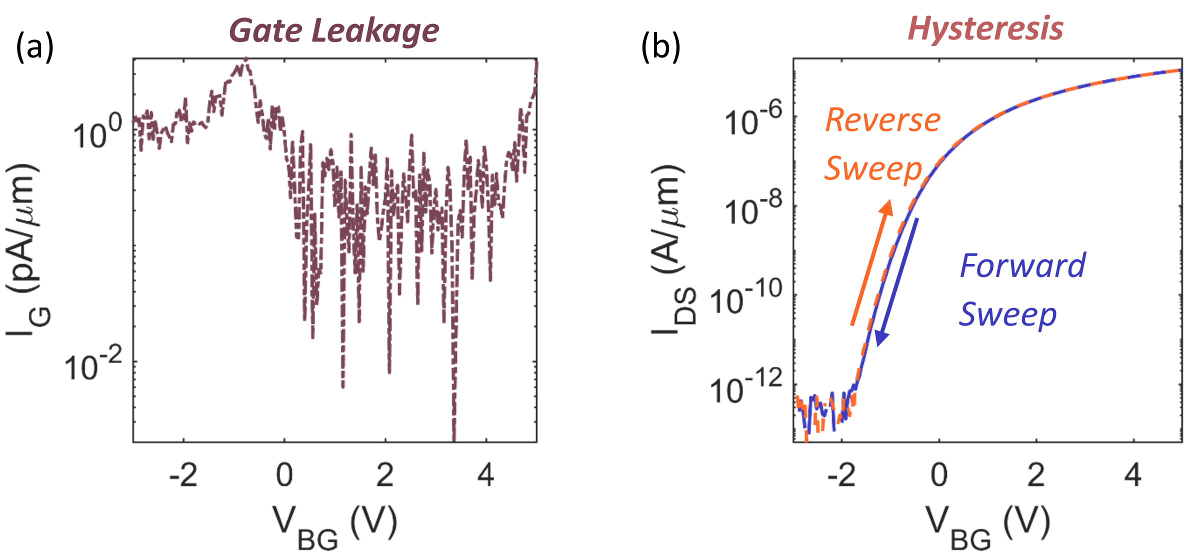

Figure S2. *a) Gate leakage characteristics of monolayer MoS_2 FET. b) Forward and reverse sweep of device transfer characteristics shows near-zero hysteresis.*

Supplementary Information 4.

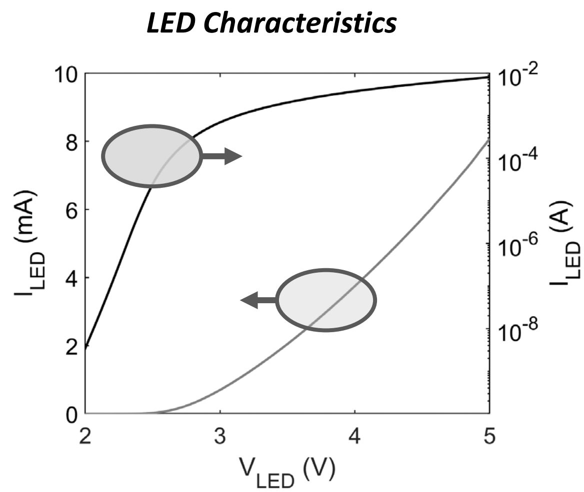

Figure S3. *Current (I_{LED}) versus voltage (V_{LED}) characteristics of the blue LED used in our experiments as the visual stimuli is shown in the logarithmic and linear scale.*

Supplementary Information 5.

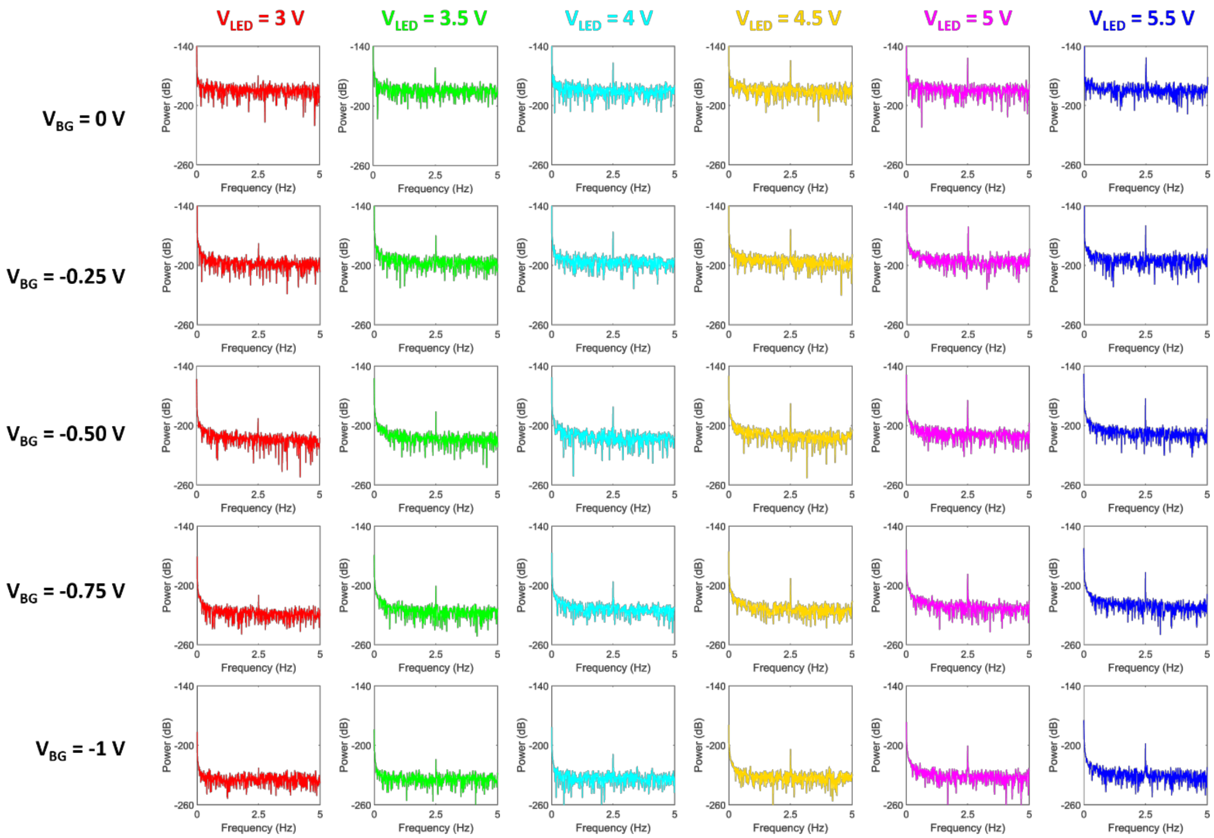

Figure S4. *Power spectral density (PSD) obtained using the Fast Fourier Transform (FFT) of the output current of the monolayer* MoS_2 *photodetector corresponding to 2.5 Hz periodic LED signals of different amplitudes (*V_{LED}*) at different back-gate voltages (*V_{BG}*). The peak at 2.5Hz confirms successful detection of the visual stimuli.*

Supplementary Information 6.

The photogating effect is explained using the energy band diagrams along the current transport (Fig. S5a) and gate electrostatic (Fig. S5b) directions in the MoS_2 FET in the ON-state, subthreshold and OFF state. Under the illumination of the blue LED (450 – 500 nm), electron-hole pairs are generated in the MoS_2 channel since the incident photon energy exceeds ~1.84 eV, the bandgap of monolayer MoS_2. These photoexcited carriers drift towards the respective metal electrodes under the applied source to drain bias (V_{DS} = 1 V) constituting the photocurrent that adds to the FET dark current (upper panel – left diagram). In the ON state, the photocurrent is mostly independent of V_{BG} (Fig. 2a) and is also obscured by the device dark current even for the brightest LED signal. As such the SNR is significantly low and the LED signals are undetectable

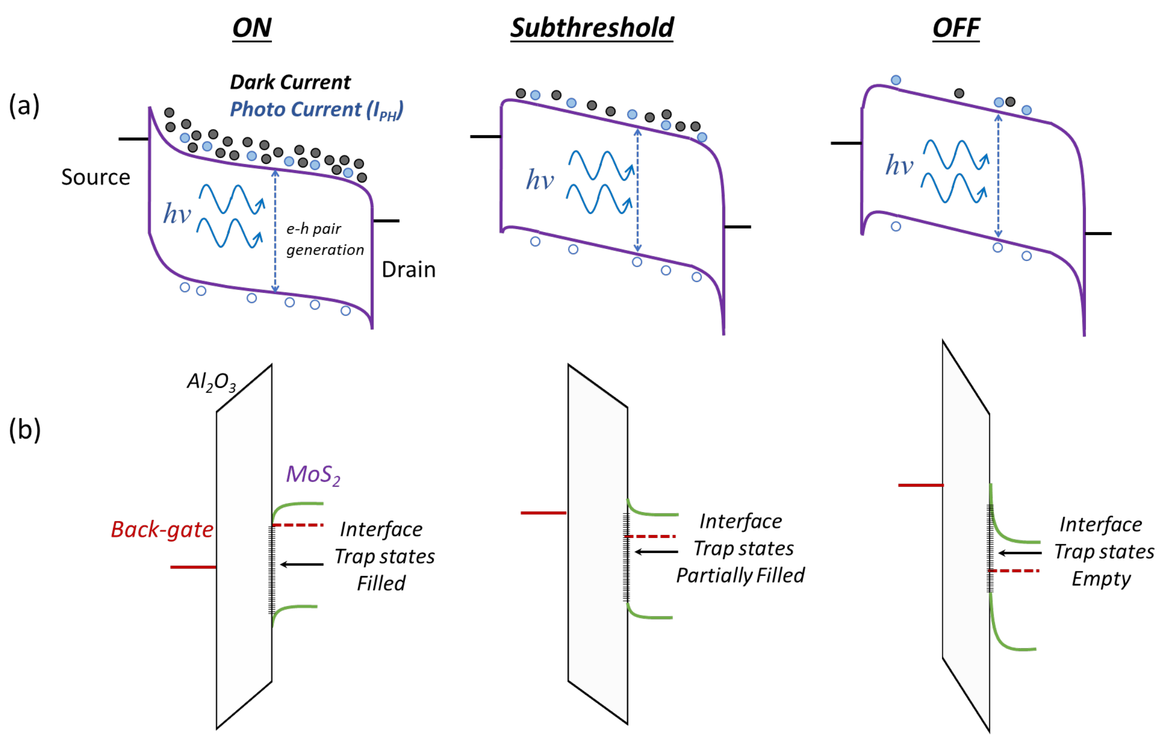

Figure S5. *a) Energy band diagrams along the current transport direction showing the electron-hole pair generation in the ON-state, Subthreshold and the OFF-state operating regimes of the device under the illumination of blue LED, along with the depiction of dark current(black) and photocurrent(blue). b) Energy band diagrams along the gate electrostatic direction showing filled interface trap states in the ON-state, partially filled interface trap states in the subthreshold and empty interface trap states in the OFF-state of the device.*

in the ON-state. By operating the device in the subthreshold, the dark current can be reduced exponentially by increasing the barrier for electron injection from the source contact (upper panel – middle diagram). This improves the SNR. However, in deep-subthreshold or OFF-state carrier trapping at the interface between Al_2O_3 and MoS_2 reduces the photocurrent significantly which makes the SNR low again (upper panel – right diagram). The origin of interface trap states can be attributed to the dangling Al−O bonds at the surface [22]. Since the photocarriers trapped in these interface states follow Fermi−Dirac distribution with the Fermi level being determined by the equilibrium Fermi level of the MoS_2 channel, less carrier trapping occurs in the ON-state (lower panel – left diagram) and more carrier trapping occurs in the subthreshold (lower panel – middle diagram) and OFF-state (lower panel – right diagram). This explains why the photocurrent keeps decreasing for negative back-gate voltages (Fig. 2a).

Supplementary Information 7.

The photogating effect can be explained further using the sweep rate dependent hysteresis measurements of MoS_2 FET in dark and under illumination. The increase in hysteresis window under illumination and with increasing sweep rate provide direct evidence that photogating effect plays a dominant role in the photoresponse of MoS_2 FET.

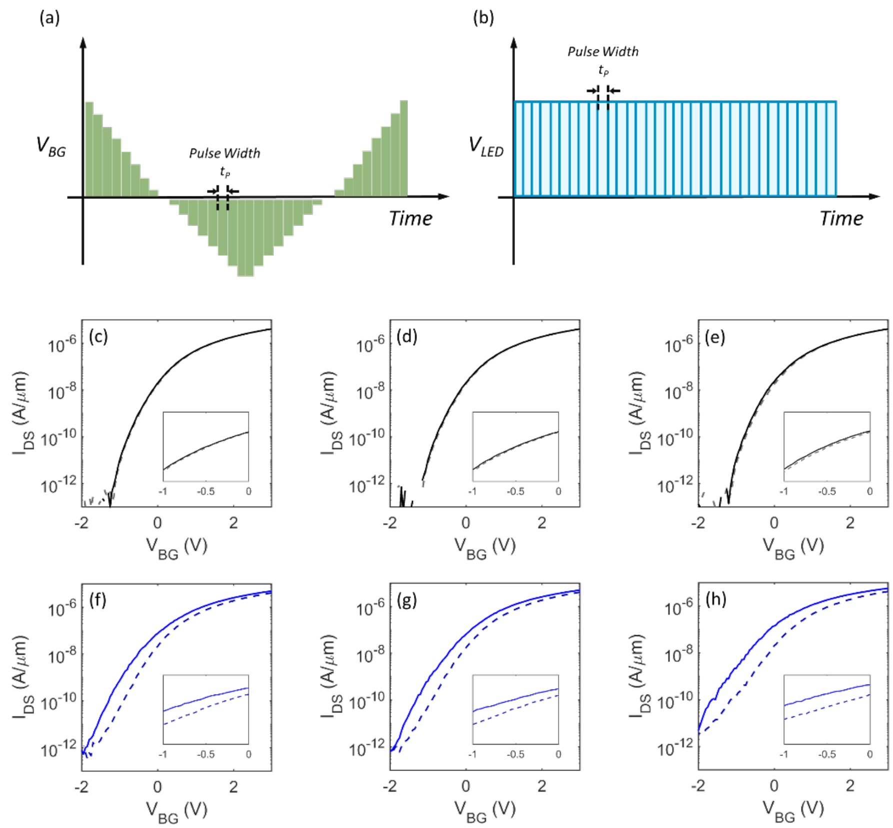

(i)

t_P (ms)	ΔV_{HW} (V) - Dark	ΔV_{HW} (V) - Light
10	0.02	0.39
100	0.02	0.40
1000	0.04	0.55

Figure S6. *a) Change in the back-gate voltage (V_{BG}) and b) LED voltage (V_{LED}) with time, during the sweep rate dependent hysteresis measurements. V_{BG} changes from positive to negative during the forward sweep and negative to positive during the reverse sweep. The voltage supplied to the LED (V_{LED}) is constant with time. V_{LED} = 5 V for hysteresis measurement under illumination. Sweep rate dependent hysteresis measurements of MoS_2 FET in dark with c) t_P = 10 ms, d) t_P = 100 ms and e) t_P = 1000 ms shows negligible hysteresis window whereas the same measurements done under a constant illumination of V_{LED} = 5V for f) t_P = 10 ms, g) t_P = 100 ms and h) t_P = 1000 ms shows an increase in the hysteresis window by an order of magnitude, for all the sweep rates. h) Hysteresis window (ΔV_{HW}) for sweep rate dependent hysteresis measurements in dark and under illumination are compared and summarized in the table. This was extracted using iso current method at I_{DS} = 1 nA.*

Supplementary Information 8.

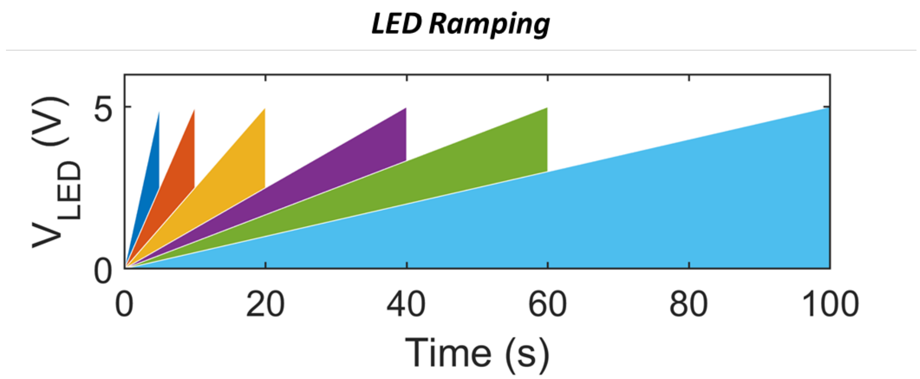

Figure S7. *LED voltage is ramped from 0 V to 5 V for different time intervals determining the rate of intensity increase in each case. This determines the speed at which the object is approaching.*

Supplementary Information 9.

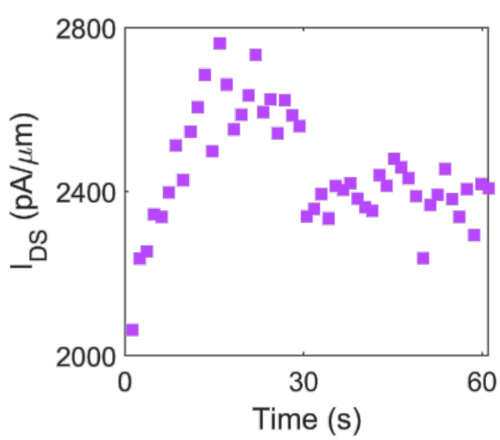

Figure S8. *Device response to a receding object stimulated by decreasing the LED intensity from 5 V to 0 V.*

Supplementary Information 10.

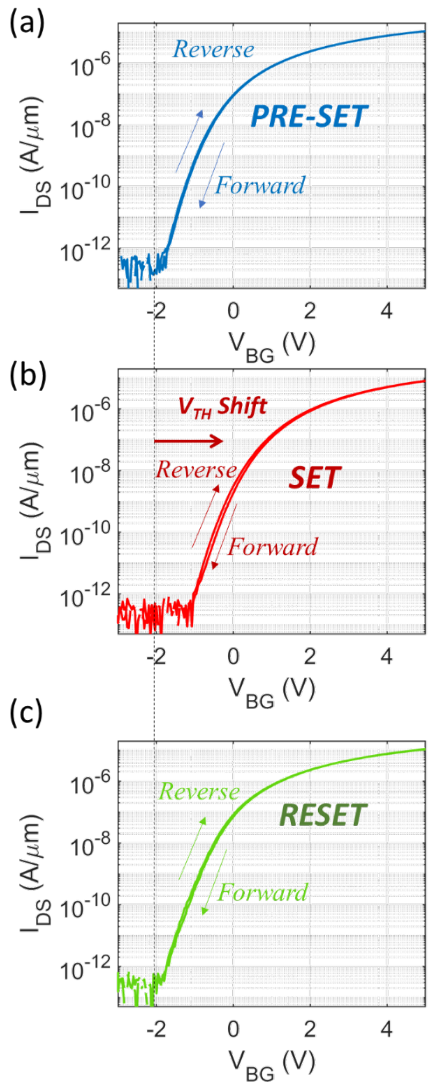

Figure S9. *a) Transfer characteristics of monolayer MoS_2 FET measured at V_{DS} = 1 V before programming (PRE-SET). The threshold voltage of the device was found to be at V_{TH} = 1 V. b) Device is electrically programmed by applying a SET voltage V_P = 7.5 V at the back gate for a duration of 75 s. Clearly, the threshold voltage shows a positive shift. c) Device is restored back to its original state by applying a RESET voltage V_P = -8 V for a duration of 100 ms. The lack of hysteresis in the transfer characteristics of our MoS_2 FET measured pre-programming (PRE-SET) post-programming (SET) and after erase (RESET) is an indication of insignificant charge trapping at the MoS_2/Al_2O_3 interface. Therefore, the shift in threshold voltage (ΔV_{TH}) due to "Write" programming pulses applied to the back-gate can only be accounted for by the fixed charges on the FG.*

Supplementary Information 11.

Note that FG architectures can offer non-volatile charge retention based on two possible mechanisms, both of which leads to change in the threshold voltage ($\Delta \boldsymbol{V_{TH}}$).

$$\Delta \boldsymbol{V_{TH}} = -\frac{\boldsymbol{Q_{IT}(\psi_s)}}{\boldsymbol{C_{ox}}} - \frac{\boldsymbol{Q_F}}{\boldsymbol{C_{ox}}} \qquad [\boldsymbol{S1}]$$

Many recent studies exploit the first term, which is related to charge trapping/de-trapping mechanisms at the semiconductor/dielectric interface to offer memory retention ranging from several minutes to days [23-26]. However, since the population of interface traps depends on the channel surface potential ($\boldsymbol{\psi_s}$), which is determined by $\boldsymbol{V_{BG}}$, these FG devices exhibit hysteresis in the transfer characteristics. The lack of hysteresis in the transfer characteristics of our MoS_2 FET measured pre- and post-programming is an indication of insignificant charge trapping at the MoS_2/Al_2O_3 interface (see ***Supplementary Information 10***). Therefore, we attribute the shift in threshold voltage ($\Delta \boldsymbol{V_{TH}}$) in our biomimetic device to the fixed charges on the FG, following Eq. S1 with $\boldsymbol{Q_{IT}} \approx \boldsymbol{0}$. As discussed earlier these fixed charges ($\boldsymbol{Q_F}$) are injected from the p^{++}-Si into the Pt/TiN FG *via* Fowler Nordheim (FN) tunneling and are stored in the FG rather than populating the interface trap states.

Supplementary Information 12.

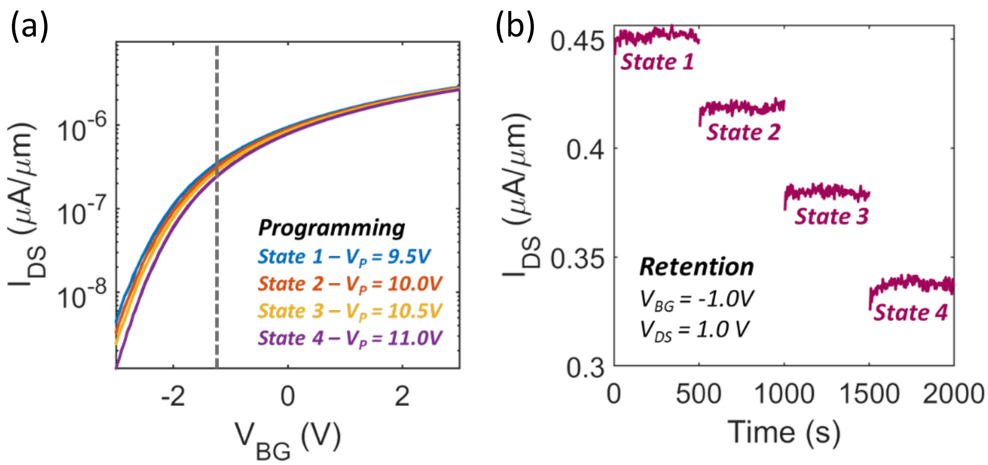

Figure S10. *a) Programming and b) retention of different analog memory states for the biomimetic device. The post-programing source to drain currents (I_{DS}) were measured for 500 s for each memory state demonstrating adequate charge retention by the floating gate stack.*

Supplementary Information 13.

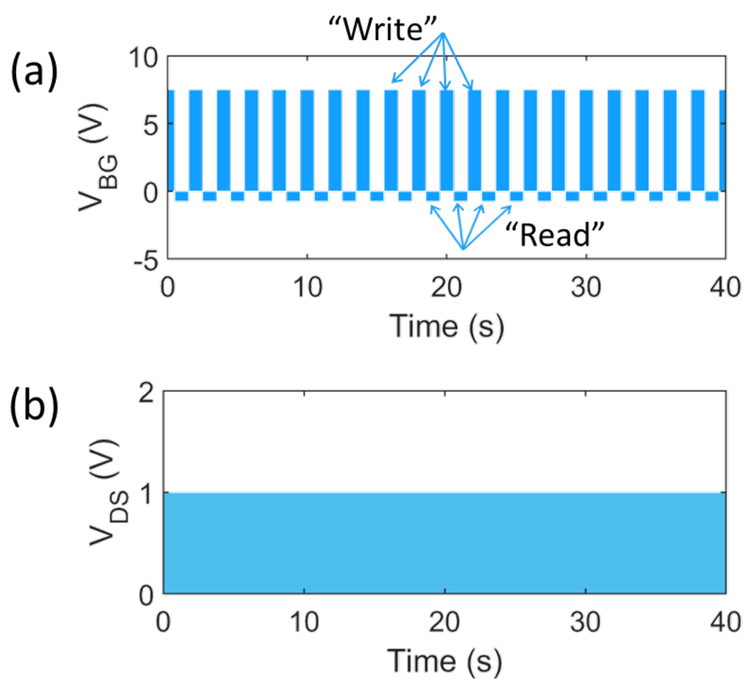

Figure S11. *a) "Read" and "Write" programming set-up for the monolayer MoS_2 FET to invoke the inhibitory response. b) V_{DS} is kept constant at 1 V.*

Supplementary Information 14.

I. Virtual Source (VS) model describing MoS_2 FET characteristics in Dark:

We have used the Virtual Source (VS) model developed for nanoscale devices by Lundstrom *et al.* [27] to describe the transfer characteristics of our back-gated MoS_2 FET in dark, as shown in Fig. S12. In VS model both the subthreshold and the above threshold FET characteristics are captured using a single semi-empirical and phenomenological relationship (Eq. S2a,b) that describes the transition in channel charge (Q_{dark}) from the ON state (strong inversion) to the OFF state (weak inversion). The model parameters are extracted from the experimental device characteristics.

$$Q_{dark} = \frac{k_B T}{q} C_{ox} m \log\left[1 + \exp\left(\frac{V_{BG} - V_{TH}}{\frac{m k_B T}{q}}\right)\right] \qquad [S2a]$$

$$G_{dark} = \frac{W \mu_N Q_{dark}}{L}; \qquad I_{DS-dark} = G_{dark} V_{DS}; \qquad [S2b]$$

Here, k_B is the Boltzmann's constant, T is the temperature set to 300 K, q is the electronic charge, C_{ox} is the back-gate oxide capacitance, m is the band movement factor, V_G is the back-gate voltage, V_{TH} is the threshold voltage, L = 1 µm is the length of the channel, W = 5 µm is the width of the channel, μ_N is the field effect electron mobility, $I_{DS-dark}$ is the source to drain dark current i.e. without any LED illumination and V_{DS} is the source to drain voltage. We calculated, C_{ox} to be $1.8\text{x}10^{-3}$ F/m^2 using the formula $C_{ox} = \varepsilon_0 \varepsilon_{ox} / t_{ox}$, where, ε_0 is the vacuum permittivity, and ε_{ox} = 10 is the relative permittivity and t_{ox} = 50 nm is the thickness of the back-gate oxide [28]. The band movement factor was extracted to be m = 5.3 from the subthreshold slope ($SS = mk_B T ln10$) and the threshold voltage was found to be V_{TH} = 0.45 V from the experimental transfer characteristics. The field effect carrier mobility for electrons in MoS_2 used for the fitting was found to be μ_N = 10 cm^2/V-s. This is different compared to the experimentally found peak mobility value of μ_N = 20 cm^2/V-s. The contact resistance was found to be significantly smaller compared to the channel resistance and hence was ignored in the VS model.

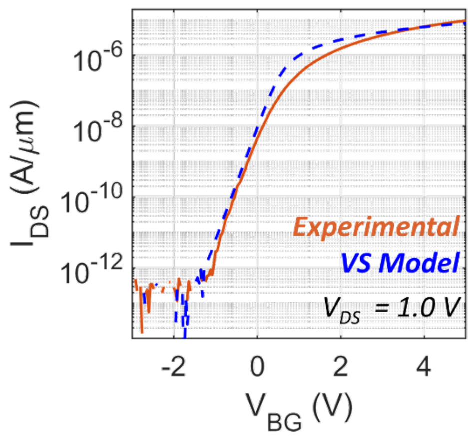

Figure S12. *Virtual Source (VS) model describing the transfer characteristics of our back-gated MoS_2 FET. In VS model both the subthreshold and the above threshold FET characteristics are captured using a single semi-empirical and phenomenological relationship that describes the transition in channel charge from the ON state (strong inversion) to the OFF state (weak inversion). The model parameters (m, V_{TH}, μ_N) are extracted from the experimental device characteristics as described in the text.*

II. Empirical model describing the LED Characteristics:

We have used an empirical model (Eq. S3) to capture the current (I_{LED}) *versus* voltage (V_{LED}) characteristics of the blue LED as shown in Fig. S13.

$$I_{LED} = I_0 \log\left[1 + \exp\left(\frac{V_{LED} - V_{LED,T}}{\frac{m_{LED}k_B T}{q}}\right)\right] \qquad [S3]$$

Here, $V_{LED,T}$ is the LED turn ON voltage, which was extracted from the linear scale LED characteristics and was found to be 2.6 V, whereas, I_0 = 1.4x10^{-4} A is a fitting parameter to match the ON current and m_{LED} = 2.1 is a fitting parameter that captures the subthreshold LED characteristics.

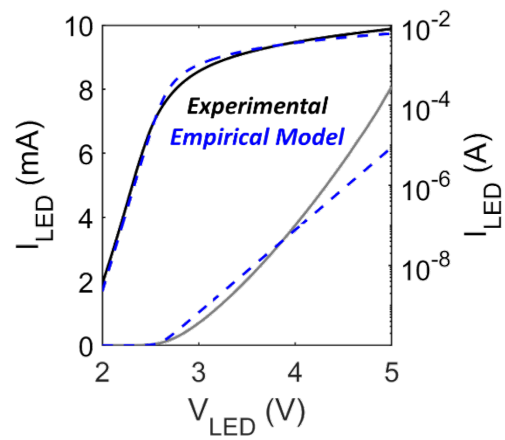

Figure S13. *Empirical model describing the LED Characteristics. The model parameters ($V_{LED,T}$, I_0, m_{LED}) are extracted from the experimental device characteristics to match the ON current and subthreshold LED characteristics.*

III. Empirical model describing the photoresponse of MoS_2 FET:

The photoconductance of MoS_2 FET depends on three factors: a) the LED intensity, which is determined by the LED current (I_{LED}), b) the operating regime of the FET, which is determined by the back-gate voltage (V_{BG}) and c) the illumination time, which is determined by the speed of the looming stimulus. Fig. S14a shows the experimentally obtained photoconductance, $G_{ph} = (I_{DS-light} - I_{DS-dark})/V_{DS}$, in MoS_2 FET as a function of the LED current (I_{LED}) and the corresponding fit using an empirical power law relationship (Eq. S4). The numerical values for the fitting parameters were found to be $\alpha = 2\text{x}10^{-6}$ and $\beta = 0.3$.

$$G_{ph} = \alpha I_{LED}^{\beta} \qquad [S4]$$

We have found that in the ON state, the experimentally extracted photoconductance (G_{ph}) is mostly independent of V_{BG} as shown in Fig. S14b. However, G_{ph} decreases exponentially when the device is biased in the subthreshold regime. This is due to the carrier trapping at the interface between Al_2O_3 and MoS_2 that significantly reduces the photocurrent. The origin of interface trap states can be attributed to the dangling Al−O bonds at the surface [22]. Since the photocarriers trapped in these interface states follow Fermi−Dirac distribution with the Fermi level being determined by the equilibrium Fermi level of the MoS_2 channel, more carrier trapping occurs in the subthreshold and OFF-state. We have used an empirical relationship (Eq. S5a, b) to fit the experimental results as shown in Fig. S14b. We have used m_{ph} = 6.5 and V_{T-ph} = 0 V for the fitting.

$$G_{ph} = \alpha I_{LED}^{\beta} \frac{m_{ph} k_B T}{q} \log\left[1 + \exp\left(\frac{V_{BG} - V_{T-ph}}{\frac{m_{ph} k_B T}{q}}\right)\right] \frac{1}{1 + log\left[1 + \exp\left(V_{BG} - V_{T-ph}\right)\right]} \quad [S5a]$$

$$G_{ph} \approx \begin{cases} \alpha I_{LED}^{\beta} & V_{BG} > V_{T-ph} \\ \alpha I_{LED}^{\beta} \frac{m_{ph} k_B T}{q} \exp\left(\frac{V_{BG} - V_{T-PH}}{\frac{m_{ph} k_B T}{q}}\right) & V_{BG} < V_{T-ph} \end{cases} \quad [S5b]$$

Note that, $\log(1 + x) \approx x \; for \; x \ll 1$

The dependence of photoconductance (G_{ph}) on the LED illumination time was studied using the response of the biomimetic device to the looming stimuli i.e. different ramp rates for the LED voltage. Fig. S14c shows the experimentally extracted photoconductance (G_{ph}) as a function of the LED pulse width (t_P) for different V_{BG}. Here, N = 101, is the number of pulses. It is found that G_{ph} follows power law dependence with t_P (Eq. S6) and the coefficients (γ, δ) change as a function of V_{BG} since back-gate voltage changes the channel surface potential which in turn determines the population of interface trap states, their nature and the trapping/detrapping time constants. These coefficients are tabulated in Fig. S14d. A detailed analysis is beyond the scope of this paper.

$$G_{ph} = \gamma t_P^{\delta} \qquad [S6]$$

Finally, Fig. S14e-h show the simulated photoresponse of the biomimetic device to looming stimuli at different V_{BG} by combining Eq. S4 through Eq. S6 with remarkable similarity with the experimental observations (Fig. 2g-j).

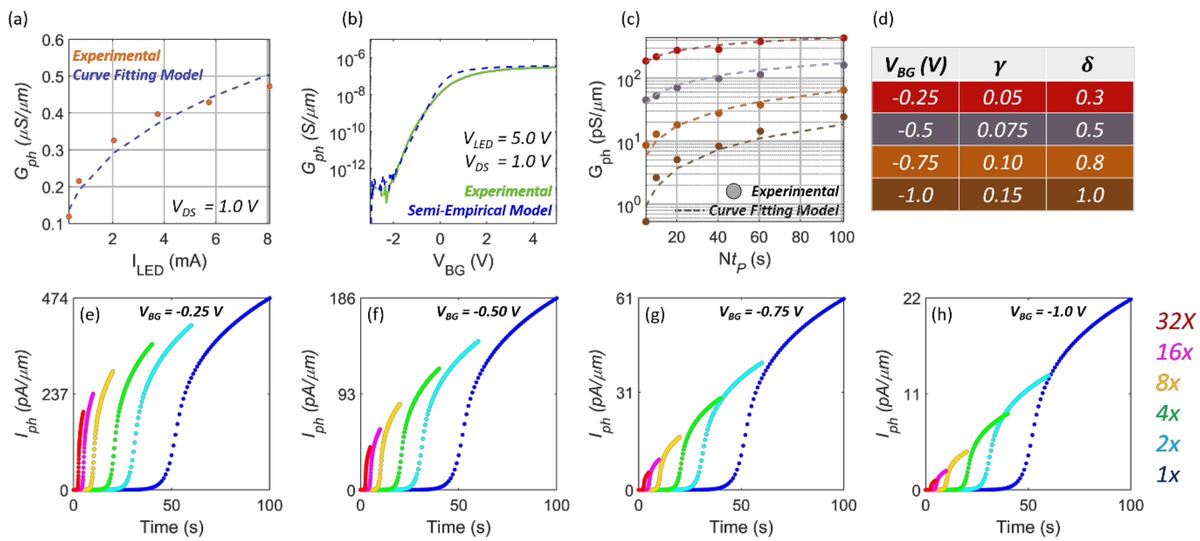

Figure S14. *Empirical model describing the photoresponse of MoS_2 FET. a) The dependence of photoconductance G_{ph} on LED intensity, which is determined by the LED current (I_{LED}). Experimental (solid circles) and the corresponding fit (blue dotted line) using an empirical power law relationship described in the text. b) The dependence of photoconductance G_{ph} on the back-gate voltage (V_{BG}). Experimental (solid green line) and the corresponding fit (blue dotted line) using an empirical relationship described in the text. c) The dependence of photoconductance G_{ph} on the illumination time, i.e. the LED pulse width (t_P) for different V_{BG}. Here, N = 101, is the number of pulses. Experimental (solid circles) and the corresponding fits (dotted line) using power law relationships described in the text. d) Table summarizing the coefficients in the power law expression which change as a function of V_{BG} since back-gate voltage changes the channel surface potential which in turn determines the population of interface trap states, their nature and the trapping/detrapping time constants. Simulated photoresponse of the biomimetic device to various speed of looming stimuli at e) V_{BG} = -0.25 V, f) V_{BG} = -0.50 V, g) V_{BG} = -0.75 V, and h) V_{BG} = -1 V showing remarkable similarity with the experimental excitatory observations.*

IV. Physics based model describing the programming response of MoS_2 FET:

The shift in the threshold voltage (ΔV_{TH}) of MoS_2 FET in response to the "Write" programming pulses (V_P) applied to the back-gate electrode is attributed to the fixed negative charges (Q_F) injected into the Pt/TiN floating gate from the p^{++}-Si and is given by Eq. S7.

$$\Delta V_{TH} = -\frac{Q_F}{C_{ox}}; \quad Q_F = J_{FN} t_P; \qquad J_{FN} = \rho V_P^2 \exp\left(-\frac{\theta}{V_P}\right) \qquad [S7]$$

Here, J_{FN} is modeled as the Fowler-Nordheim (FN) tunneling current [29] and t_P is the pulse duration. Numerical values for the fitting parameters were found to be $\rho = 10^{-5}$ and $\theta = 15$ from Fig. S15a that shows the experimentally extracted ΔV_{TH} as a function of V_P. Fig. S15b shows the experimental and simulated transfer characteristics of the MoS_2 FET after the application of

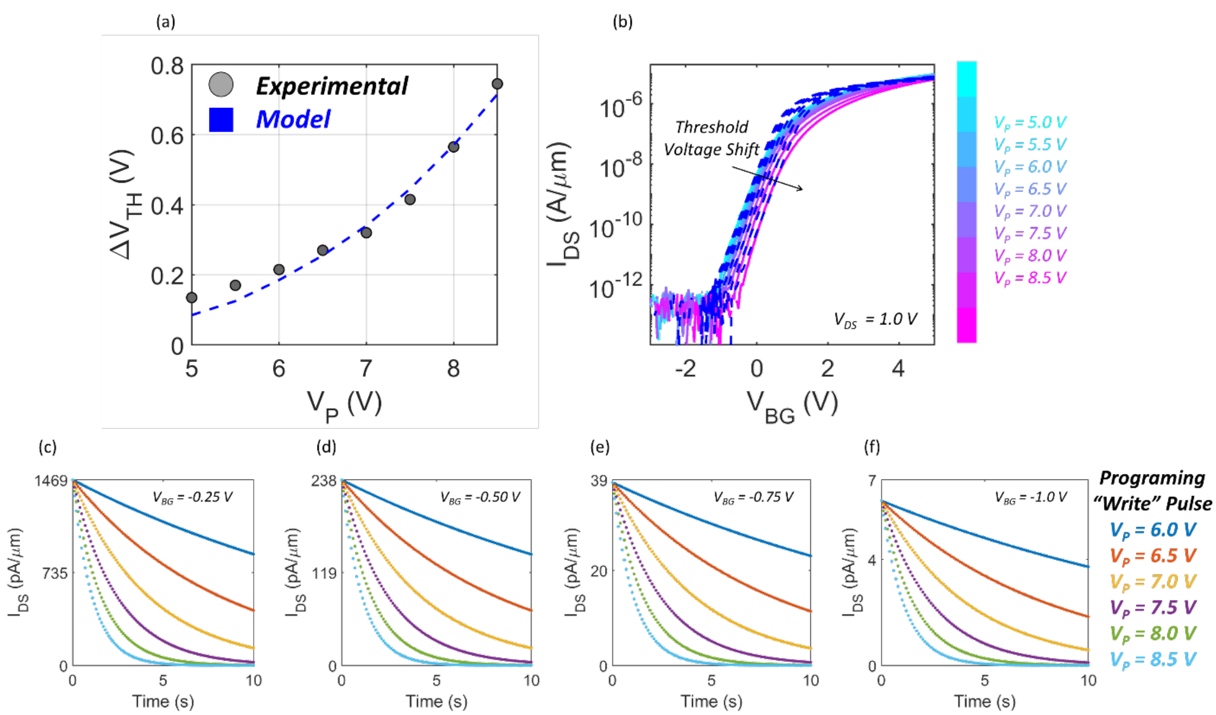

Figure S15. *Physics based model describing the programming response of MoS_2 FET. a) Experimentally extracted shift in the threshold voltage (ΔV_{TH}) as a function of the "Write" programming voltage, V_P, (solid circles) and corresponding fit using Fowler Nordheim (FN) tunneling model (dotted line). b) Experimental (solid lines) and simulated (dotted lines) transfer characteristics of the MoS_2 FET after the application of V_P of different magnitudes. c) Simulated inhibitory response to "Write" programming pulse trains with different pulse amplitudes (V_P) but constant pulse width (t_P = 100 ms) for at c) V_{BG} = -0.25 V, d) V_{BG} = -0.50 V, e) V_{BG} = -0.75 V, and f) V_{BG} = -1 V showing remarkable similarity with the experimental excitatory observations.*

"Write" programming pulses (V_P) of different magnitudes based on Eq. S1 and Eq. S7. Fig. S15c-f show the simulated inhibitory response to "Write" programming pulse trains with different pulse amplitudes (V_P) but constant pulse width (t_P = 100 ms) for different back gate biasing (V_{BG}) different back-gate biasing, which bears remarkable similarity with the experimental observations (Fig. 3d-g).

V. Simulation results for biomimetic collision detector:

Here, we combine the models described in Eq. S2 through Eq. S7 to simulate the escape response of MoS_2 FET based biomimetic collision detector. Fig. S16 show that when both the excitatory looming stimuli and inhibitory programming stimuli are presented simultaneously, the device exhibits a non-monotonic trend in the source to drain current irrespective of the speed of the object on collision course or the biasing regime resembling the experimental findings (Fig. 4a). The non-monotonic escape response can be attributed to the fact that the conductance of the device has two components: the dark conductance, which decreases due to the shift in threshold voltage caused by the programming pulse train (V_P = 7.5 V, t_P = 200 ms) following Eq. S2 and Eq. S7 and the photoconductance, which increases due to the visual excitation following Eq. S4, Eq. S5 and Eq. S6. Due to the additive nature of the two conductance values (Eq. S8), the inflection point or the time at which output current reaches the local minima occurs when the photoexcitation becomes more than the programming inhibition.

$$I_{DS}(t) = V_{DS}\left[G_{ph}(t) \uparrow + G_{dark}(t) \downarrow\right];\ G_{ph}(t) = F\{V_{LED}(t), V_{BG}\};\ G_{dark}(t) = F\{V_P, t_P\}; \qquad [S8]$$

For faster moving objects the LED reaches its peak intensity (I_{LED}) earlier and hence the inflection point occurs earlier while for slower moving objects the LED reaches its peak intensity (I_{LED}) later and hence the inflection point occurs later. However, in all instances, the inflection point in the I_{DS}

versus t characteristics occurs before the V_{LED} reaches its peak value and hence the device can be used as an impending collision indicator.

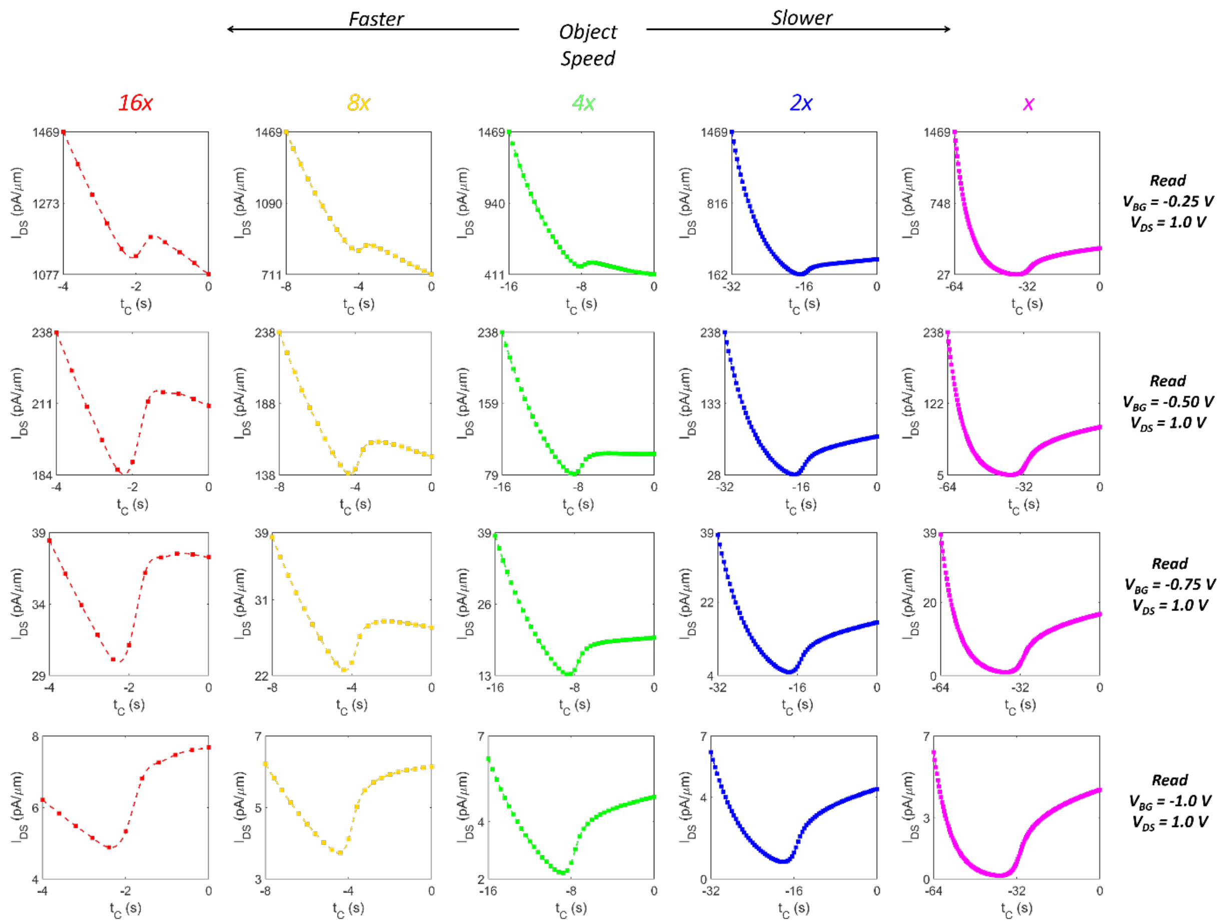

Figure S16. *Simulated escape response of MoS_2 FET based biomimetic collision detector when both the excitatory looming stimuli and inhibitory programming stimuli are presented simultaneously. The device exhibits a non-monotonic trend in the source to drain current irrespective of the speed of the object on collision course or the biasing regime resembling the experimental findings. The non-monotonic escape response can be attributed to the fact that the conductance of the device has two components: the dark conductance, which decreases due to the shift in threshold voltage caused by the programming pulse train (V_P = 7.5 V, t_P = 200 ms) and the photoconductance, which increases due to the visual excitation. Due to the additive nature of the two conductance values, the inflection point or the time at which output current reaches the local minima occurs when the photoexcitation becomes more than the programming inhibition. For faster moving objects the LED reaches its peak intensity (I_{LED}) earlier and hence the inflection point occurs earlier while for slower moving objects the LED reaches its peak intensity (I_{LED}) later and hence the inflection point occurs later.*

Supplementary Information 15.

We simulated the escape response of a 128 X 128 2D array of collision detectors. The looming stimuli is presented as a sequence of gray scale images with 128 X 128 pixels such that each pixel excites the corresponding collision detector. The pixel intensities range from black (0), when the object is far away from collision to white (255), at collision as shown in Fig. S17a. The intensities of the pixels are mapped to the LED voltages (V_{LED}) with the highest pixel intensity representing V_{LED}= 5 V. The speed of the approaching object is captured by the number of frames per second. Fig. S17b shows corresponding source to drain current maps of the 2D collision detector array (normalized to gray scale). Fig. S17c shows the non-monotonic current response from each pixel. Clearly, the current map becomes the brightest before the looming stimulus reaches the peak intensity allowing collision avoidance. ***Supplementary Video File 5*** also shows the looming stimuli, corresponding source to drain current maps of the 2D collision detector array (normalized to gray scale) and the escape responses. Since the monotonic increase in the image intensity

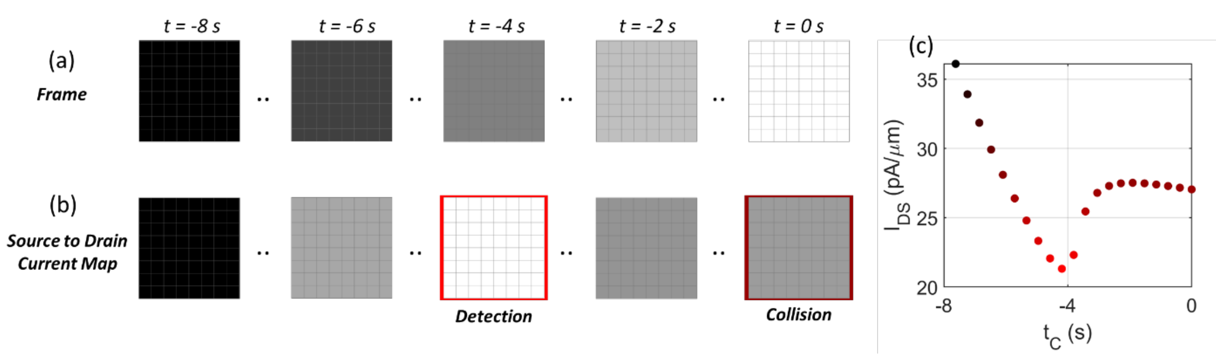

Figure S17. *Simulated the escape response from a multipixel collision detector comprising of 128 X 128 2D array of collision detectors. a) The looming stimuli is presented as a sequence of gray scale images with 128 X 128 pixels such that each pixel excites the corresponding collision detector. The pixel intensities range from black (0), when the object is far away from collision to white (255), at collision. The intensities of the pixels are mapped to the LED voltages (V_{LED}) with the highest pixel intensity representing V_{LED}= 5 V. The speed of the approaching object is captured by the number of frames per second. b) Source to drain current maps of the 2D collision detector array (normalized to gray scale). Clearly, the current map becomes the brightest before the looming stimulus reaches the peak intensity allowing collision avoidance. c) Monotonic increase in the image intensity invokes non-monotonic response in the source to drain current for all the individual collision detectors in the 2D array.*

invokes non-monotonic response in the source to drain current for all the individual collision detectors in the 2D array, the current maps and the pixel responses show non-monotonic trends as a function of time with the inflection points occurring before the impending collision. This is very similar to the trend observed from the response of a single device to an approaching object in direct collision course. Therefore, unlike other vision sensors, where the absence of non-monotonic response from the individual photodetectors necessitates the use of an array and associated peripheral circuitry to determine the optic flow, our biomimetic collision detector can avoid the use of such an array providing tremendous area and energy benefits.

However, there can be other benefits of using an array of our biomimetic collision detectors. In our experimental demonstration, the biomimetic collision detector can identify an impending collision, but it is unable to determine the direction from which the object is approaching. This information is critical for determining the escape response, e.g. the angle of escape flight for the locust. While a single device cannot resolve the directionality of the collision, a 2D array of the detectors can extract such information when used in conjunction with an optical lens. As shown in Fig. S18, by placing the 2D array of collision detector at the focal plane of the lens it is possible to enable a 3D vision for collision avoidance. For perpendicular incidence, the collision detector at the focal point of the lens is excited, whereas, for oblique incidence at an angle θ, specific detectors in the array is excited, thereby creating a 2D map along the focal plane of the lens. This demonstration shows the mapping of 3D space onto the 2D array of collision detectors using an optical lens, therefore making the biomimetic collision detector to be direction sensitive. The response map of collision detectors in the array can thus help in determining the velocity and direction of an approaching object, both of which are critical in the detection of impending collisions.

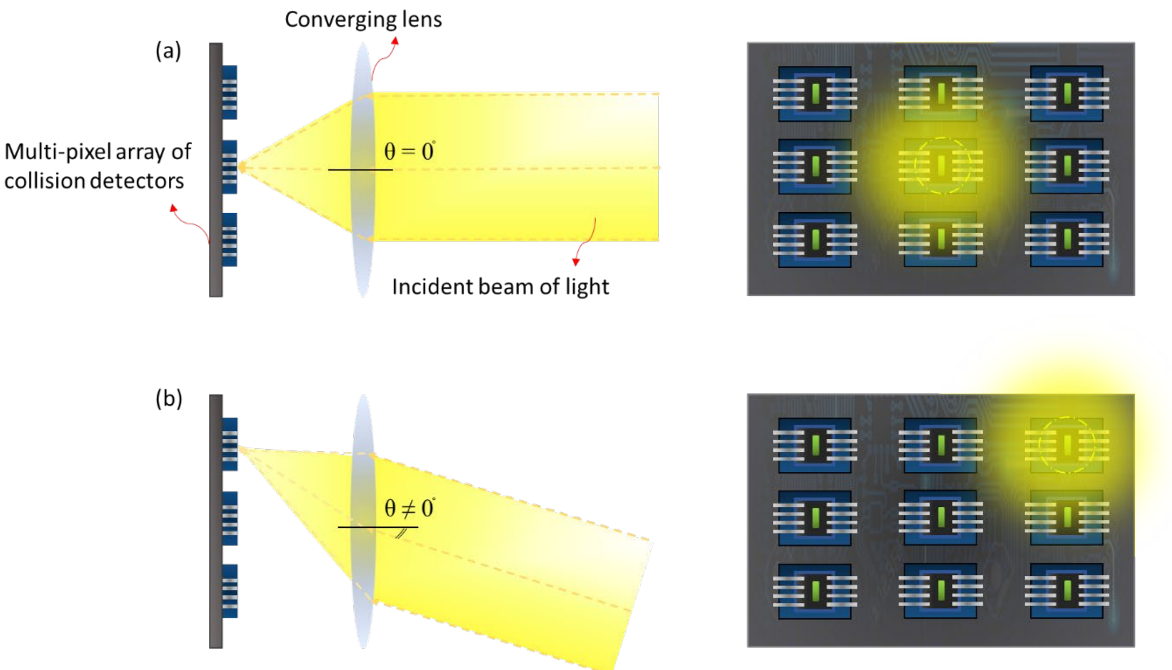

Figure S18. *Multipixel 2D array of biomimetic collision detector can resolve the directionality of the impending collision, a critical information necessary for determining the escape response, e.g. the angle of escape flight. The 2D array of collision detectors is placed at the focal plane of a lens. For a) perpendicular incidence, the collision detector at the focal point of the lens is excited, whereas, for b) oblique incidence at an angle θ, specific detectors in the array is excited, thereby creating a 2D map of the 3D space along the focal plane of the lens.*

References

[1] J. Tanner and C. Mead, "An integrated analog optical motion sensor," 1986.

[2] A. G. Andreou and K. Strohbehn, "Analog VLSI implementation of the Hassenstein-Reichardt-Poggio models for vision computation," in *1990 IEEE International Conference on Systems, Man, and Cybernetics Conference Proceedings*, 1990, pp. 707-710.

[3] R. R. Harrison and C. Koch, "A robust analog VLSI motion sensor based on the visual system of the fly," *Autonomous robots,* vol. 7, pp. 211-224, 1999.

[4] D. Abbott, A. Moini, A. Yakovleff, X. T. Nguyen, A. Blanksby, G. Kim*, et al.*, "New VLSI smart sensor for collision avoidance inspired by insect vision," in *Intelligent vehicle highway systems*, 1995, pp. 105-115.

[5] A. Moini, A. Bouzerdoum, K. Eshraghian, A. Yakovleff, X. T. Nguyen, A. Blanksby*, et al.*, "An insect vision-based motion detection chip," *IEEE Journal of Solid-State Circuits,* vol. 32, pp. 279-284, 1997.

[6] A. Moini, A. Bouzerdoum, A. Yakovleff, and K. Eshraghian, "Two-dimensional motion detector based on insect vision," in *Advanced Focal Plane Arrays and Electronic Cameras*, 1996, pp. 146-157.

[7] H. Okuno and T. Yagi, "A mixed analog–digital vision sensor for detecting objects approaching on a collision course," *Robotics and Autonomous Systems,* vol. 57, pp. 508-516, 2009.

[8] R. Takami, K. Shimonomura, S. Kameda, and T. Yagi, "An image pre-processing system employing neuromorphic 100/spl times/100 pixel silicon retina [robot vision applications]," in *2005 IEEE International Symposium on Circuits and Systems*, 2005, pp. 2771-2774.

[9] R. R. Harrison, "A biologically inspired analog IC for visual collision detection," *IEEE Transactions on Circuits and Systems I: Regular Papers,* vol. 52, pp. 2308-2318, 2005.

[10] M. Sarkar, D. S. S. Bello, C. van Hoof, and A. J. Theuwissen, "Biologically inspired CMOS image sensor for fast motion and polarization detection," *IEEE Sensors Journal,* vol. 13, pp. 1065-1073, 2012.

[11] C. Zhang, S. Lindner, I. M. Antolovic, M. Wolf, and E. Charbon, "A CMOS SPAD imager with collision detection and 128 dynamically reallocating TDCs for single-photon counting and 3D time-of-flight imaging," *Sensors,* vol. 18, p. 4016, 2018.

[12] S. Das, J. A. Robinson, M. Dubey, H. Terrones, and M. Terrones, "Beyond Graphene: Progress in Novel Two-Dimensional Materials and van der Waals Solids," *Annual Review of Materials Research, Vol 45,* vol. 45, pp. 1-27, 2015.

[13] G. R. Bhimanapati, Z. Lin, V. Meunier, Y. Jung, J. Cha, S. Das*, et al.*, "Recent Advances in Two-Dimensional Materials beyond Graphene," *ACS Nano,* vol. 9, pp. 11509-11539, 2015/12/22 2015.

[14] S. Manzeli, D. Ovchinnikov, D. Pasquier, O. V. Yazyev, and A. Kis, "2D transition metal dichalcogenides," *Nature Reviews Materials,* vol. 2, p. 17033, 2017.

[15] K. F. Mak and J. Shan, "Photonics and optoelectronics of 2D semiconductor transition metal dichalcogenides," *Nature Photonics,* vol. 10, p. 216, 2016.

[16] K. Kang, S. Xie, L. Huang, Y. Han, P. Y. Huang, K. F. Mak*, et al.*, "High-mobility three-atom-thick semiconducting films with wafer-scale homogeneity," *Nature,* vol. 520, p. 656, 2015.

[17] T. H. Choudhury, H. Simchi, R. l. Boichot, M. Chubarov, S. E. Mohney, and J. M. Redwing, "Chalcogen precursor effect on cold-wall gas-source chemical vapor deposition growth of WS2," *Crystal Growth & Design,* vol. 18, pp. 4357-4364, 2018.
[18] F. Zhang, C. Erb, L. Runkle, X. Zhang, and N. Alem, "Etchant-free transfer of 2D nanostructures," *Nanotechnology,* vol. 29, p. 025602, Jan 12 2018.
[19] H. Li, Q. Zhang, C. C. R. Yap, B. K. Tay, T. H. T. Edwin, A. Olivier*, et al.*, "From Bulk to Monolayer MoS2: Evolution of Raman Scattering," *Advanced Functional Materials,* vol. 22, pp. 1385-1390, Apr 10 2012.
[20] S. Das, H. Y. Chen, A. V. Penumatcha, and J. Appenzeller, "High performance multilayer MoS2 transistors with scandium contacts," *Nano Lett,* vol. 13, pp. 100-5, Jan 09 2013.
[21] D. S. Schulman, A. J. Arnold, and S. Das, "Contact engineering for 2D materials and devices," *Chem Soc Rev,* Mar 2 2018.
[22] M. M. Furchi, D. K. Polyushkin, A. Pospischil, and T. Mueller, "Mechanisms of photoconductivity in atomically thin MoS2," *Nano letters,* vol. 14, pp. 6165-6170, 2014.
[23] J. Lee, S. Pak, Y.-W. Lee, Y. Cho, J. Hong, P. Giraud*, et al.*, "Monolayer optical memory cells based on artificial trap-mediated charge storage and release," *Nature communications,* vol. 8, pp. 1-8, 2017.
[24] A. J. Arnold, A. Razavieh, J. R. Nasr, D. S. Schulman, C. M. Eichfeld, and S. Das, "Mimicking Neurotransmitter Release in Chemical Synapses via Hysteresis Engineering in MoS2 Transistors," *ACS nano,* vol. 11, pp. 3110-3118, 2017.
[25] M. Sup Choi, G.-H. Lee, Y.-J. Yu, D.-Y. Lee, S. Hwan Lee, P. Kim*, et al.*, "Controlled charge trapping by molybdenum disulphide and graphene in ultrathin heterostructured memory devices," *Nature Communications,* vol. 4, p. 1624, 2013/03/27 2013.
[26] T. Paul, T. Ahmed, K. K. Tiwari, C. S. Thakur, and A. Ghosh, "A high-performance MoS2 synaptic device with floating gate engineering for neuromorphic computing," *2D Materials,* vol. 6, p. 045008, 2019.
[27] M. S. Lundstrom and D. A. Antoniadis, "Compact models and the physics of nanoscale FETs," *IEEE Transactions on Electron Devices,* vol. 61, pp. 225-233, 2014.
[28] V. K. Singh, R. Pendurthi, J. R. Nasr, H. Mamgain, R. S. Tiwari, S. Das*, et al.*, "Study on the Growth Parameters and the Electrical and Optical Behaviors of 2D Tungsten Disulfide," *ACS Applied Materials & Interfaces,* vol. 12, pp. 16576-16583, 2020/04/08 2020.
[29] M. Lenzlinger and E. Snow, "Fowler-Nordheim tunneling into thermally grown SiO2," *Journal of Applied physics,* vol. 40, pp. 278-283, 1969.